

1 **Quantifying the migration rate of drainage divides from**  
2 **high-resolution topographic data**

3 Chao Zhou<sup>1</sup>, Xibin Tan<sup>2,\*</sup>, Yiduo Liu<sup>2</sup>, Feng Shi<sup>1,3</sup>

4 <sup>1</sup> State Key Laboratory of Earthquake Dynamics, Institute of Geology, China  
5 Earthquake Administration, Beijing 100029, China

6 <sup>2</sup> Key Laboratory of Mountain Hazards and Surface Processes, Institute of Mountain  
7 Hazards and Environment, Chinese Academy of Sciences, Chengdu 610299, China

8 <sup>3</sup> Shanxi Taiyuan Continental Rift Dynamics National Observation and Research  
9 Station, Beijing 100029, China

10 \*Corresponding author. E-mail address: tanxibin@imde.ac.cn

11 **Abstract**

12 The lateral movement of drainage divides is co-influenced by tectonics,  
13 lithology, and climate, and therefore archives a wealth of geologic and climatic  
14 information. It also has wide-ranging implications for topography, the sedimentary  
15 record, and biological evolution, thus has drawn much attention in recent years.  
16 Several methods have been proposed to determine drainage divides' migration state  
17 (direction and rate), including geochronological approaches (e.g., <sup>10</sup>Be) and  
18 topography-based approaches (e.g.,  $\chi$ -plots or Gilbert metrics). A key object in these  
19 methods is the channel head, which separates the hillslope and channel. However, due  
20 to the limited resolution of topography data, the required channel-head parameters in  
21 the calculation often cannot be determined accurately, and empirical values are used

22 in the calculation, which may induce uncertainties. Here, we propose two methods to  
23 calculate the migration rate of drainage divides, based on the relatively accurate  
24 channel-head parameters derived from high-resolution topographic data. We then  
25 apply the methods to an active rift shoulder (Wutai Shan) in the Shanxi rift, and a  
26 tectonically stable area (Yingwang Shan) in the Loess Plateau, to illustrate how to  
27 calculate drainage-divide migration rates. Our results show that the Wutai Shan  
28 drainage divide is migrating northwestward at a rate between 0.21 to 0.27 mm/yr,  
29 whereas the migration rates at the Yingwang Shan are approximately zero. This study  
30 indicates that the drainage-divide stability can be determined more accurately using  
31 high-resolution topographic data. Furthermore, this study takes the cross-divide  
32 differences in the uplift rate of channel heads into account in the measurement of  
33 drainage-divide migration rate for the first time.

## 34 **Keywords**

35 Drainage divide; Migration rate; High-resolution topographic data; DEM; Channel  
36 head

## 37 **1. Introduction**

38 The evolution of the Earth's surface is jointly controlled by tectonics, lithology,  
39 and climatic conditions (e.g., [Molnar and England, 1990](#); [Whipple, 2009](#); [Gallen,](#)  
40 [2018](#); [Bernard et al., 2021](#); [Hoskins et al., 2023](#)), providing a basis for reconstructing  
41 the past tectonic ([Pritchard et al., 2009](#); [Kirby and Whipple, 2012](#); [Shi et al., 2021](#)) or

42 climatic processes (Tucker and Slingerland, 1997; Hancock et al., 2002; Schildgen et  
43 al., 2022) through topography. The evolution of unglaciated terrestrial terrains is  
44 fundamentally coupled with changes in drainage systems through river's vertical  
45 (changes in river long profile) and lateral movements (drainage divide migration and  
46 river captures) (Whipple, 2001; Clark et al., 2004; Bonnet, 2009; Willett et al., 2014).  
47 Previous studies have extensively investigated how river channel profiles respond to  
48 tectonic uplift (Whipple, 2001; Crosby and Whipple, 2006; Kirby and Whipple,  
49 2012), lithological differences (Duvall et al., 2004; Safran et al., 2005; Forte et al.,  
50 2016), and precipitation perturbations (Schlunegger et al., 2011; Bookhagen and  
51 Strecker, 2012). River long profiles have been used to study earthquake events (e.g.,  
52 Burbank and Anderson, 2001; Wei et al., 2015) and the spatio-temporal variations of  
53 uplift (e.g., Whipple et al., 1999; Kirby et al., 2003; Pritchard et al., 2009; Goren et  
54 al., 2014). Recent studies show that the widespread lateral movement of river basins  
55 driven by geological and/or climatic disturbance (Yang et al., 2019; Zondervan et al.,  
56 2020; Zhou et al., 2022a; Bian et al., 2024) also interacts with the adjustment of  
57 channel profiles (Willett et al., 2014). Drainage-divide migration, one form of river  
58 lateral movement, may not only carry information on geological and/or climatic  
59 disturbance (Su et al., 2020; Zondervan et al., 2020; He et al., 2021; Shi et al., 2021;  
60 Zhou et al., 2022a; Zeng and Tan, 2023) but also influence the extraction of tectonic  
61 information from channel profiles (Goren et al., 2014; Ma et al., 2020; Jiao et al.,  
62 2022). Moreover, it has multi-facet consequences for landscape evolution  
63 (Scheingross et al., 2020; Stokes et al., 2023), sedimentary processes (Clift &

64 [Blusztajn, 2005; Willett et al., 2018; Deng et al., 2020; Zhao et al., 2021](#)), and  
65 biological evolution ([Waters et al., 2001; Zemplak et al., 2008; Hoorn et al., 2010;](#)  
66 [Musher et al., 2021](#)). For this reason, the stability of drainage divides has drawn more  
67 and more attention in recent years (e.g., [Authemayou et al., 2018; Vacherat et al.,](#)  
68 [2018; Chen et al., 2021; Shelef and Goren, 2021; Sakashita and Endo, 2023; Bian et](#)  
69 [al., 2024](#)).

70 Drainage-divide migration is essentially controlled by the cross-divide  
71 difference in erosion and topographic slope ([Beeson et al., 2017; Dahlquist et al.,](#)  
72 [2018; Chen et al., 2021; Zhou et al., 2022a](#)). The erosion rates are routinely derived  
73 from geochronological techniques, such as cosmogenic nuclides (e.g.,  $^{10}\text{Be}$ )  
74 concentration measurements ([Mandal et al., 2015; Struth et al., 2017; Young and](#)  
75 [Hilley, 2018; Sassolas-Serrayet et al., 2019](#)), which can be used to calculate the  
76 migration rates of drainage divides ([Beeson et al., 2017; Godard et al., 2019; Hu et al.,](#)  
77 [2021](#)). However, these techniques are usually based on samples collected from a  
78 catchment outlet that is several, or even tens of, kilometers away from the drainage  
79 divide and thus may not represent the erosion rates close to the drainage divide  
80 ([Sassolas-Serrayet et al., 2019; Zhou et al., 2022a](#)). Besides, the high cost of sample  
81 processing makes it challenging to determine the drainage divide's motion by  
82 measuring the erosion rates throughout the large landscapes. Hence, it would be ideal  
83 to find an accessible and efficient method that can be applied to the entire landscape  
84 and make full use of the  $^{10}\text{Be}$ -derived erosion rates.

85 The advancement of the digital elevation model (DEM) has promoted the

86 development of geomorphic analysis, making it possible to determine the drainage  
87 divide's transient motion through topography analysis. For example, Willett et al.  
88 (2014) applied the  $\chi$  method to map the dynamic state of river basins. Forte and  
89 Whipple (2018) proposed the cross-divide comparison of "Gilbert metrics" (including  
90 channel heads' relief, slope, and elevation) to determine a drainage divide's migration  
91 direction. Others adopted the comparison of slope angle or relief of the hillslopes  
92 across a drainage divide to deduce its stability (Scherler and Schwanghart, 2020; Ye et  
93 al., 2022; Zhou et al., 2022b). These geomorphic techniques, so far, could only  
94 determine the migration direction of drainage divides. Braun (2018) provided an  
95 equation that considers both alluvial and fluvial areas to calculate the migration  
96 velocity of an escarpment (also a drainage divide). Zhou et al. (2022a) developed a  
97 technique to calculate the migration rate through the high base-level  $\chi$  values on both  
98 sides of a drainage divide. These new approaches require channel-head parameters to  
99 calculate the migration rate. However, the location of the channel heads sometimes  
100 cannot be accurately identified because of the limitation in the resolution of DEMs in  
101 natural cases. For this reason, empirical values of channel-head parameters are used in  
102 these studies, which may induce uncertainties.

103 This study aims to establish an approach to derive the migration rate of drainage  
104 divides, at a high precision and low cost, based on topographic analysis. We choose a  
105 tectonically active area (i.e., the Wutai Shan in the Shanxi Rift) and a tectonically  
106 inactive area (i.e., the Yingwang Shan in the Loess Plateau) to demonstrate how to  
107 quantify drainage-divide migration rates (Fig. 1). We use the aerial photography

108 acquired by unmanned aerial vehicles (UAVs) and the Structure from Motion (SfM)  
109 technology to obtain the high-resolution DEM data of these two areas (0.67 m and  
110 0.84 m spatial resolution in the Wutai Shan and the Yingwang Shan, respectively).  
111 Benefiting from the high-resolution data, the location of channel heads can be  
112 identified more accurately. We then develop two methods to calculate the drainage-  
113 divide migration rates. One is based on the measured channel-head parameters, and  
114 the other is based on an improved method of Zhou et al (2022a). Combining with the  
115 geological and low-temperature thermochronology studies of the Wutai Shan  
116 (Middleton et al., 2017; Clinkscales et al., 2020), we also quantify the cross-divide  
117 difference in uplift rates to improve the precision of drainage-divide migration rate.

118

## 119 **2. Methods**

### 120 **2.1 Channel-head-point method**

121 According to the detachment-limited stream power model (Howard and Kerby,  
122 1983; Howard, 1994), the channel's erosion rate ( $E$ ) can be expressed as:

$$123 \quad E = KA^mS^n \quad (1)$$

124 where  $K$  is the erosion coefficient,  $A$  is the upstream drainage area,  $S$  is the gradient of  
125 the river channel, and  $m$  and  $n$  are empirical constants.

126 Because of thresholds such as erosion threshold (the shear stress of overland flow  
127 must exceed the threshold of the cohesion of bed material to generate river incision)  
128 (Howard and Kerby, 1983; Perron et al., 2008) or landslide threshold (landslides

129 occur when the threshold of soil or rock strength is exceeded in high relief region)  
130 (Burbank et al., 1996; Tucker and Bras, 1998), river channels (following Eq. 1)  
131 emerge at a certain distance from the drainage divide. The region between the channel  
132 head and the drainage divide is referred to as the hillslope area, where the erosion is  
133 controlled by landslide, collapse, and diffusion processes (Carson and Kirkby, 1972;  
134 Stock and Dietrich, 2006; Stark, 2010; Braun et al., 2018; Dahlquist et al., 2018). The  
135 channel-head point is the highest and the closest point to the drainage divide on a  
136 river channel (Clubb et al., 2014). Therefore, the erosion rate at channel-head points  
137 ( $E_{ch}$ ) can be described as:

$$138 \quad E_{ch} = KA_{cr}^m S_{ch}^n \quad (2)$$

139 where  $E_{ch}$  is the erosion rate at channel-head points,  $A_{cr}$  is the critical upstream  
140 drainage area of a channel-head point (Duvall et al., 2004; Wobus et al., 2006), and  
141  $S_{ch}$  is the channel-head gradient measured along the channel near the channel-head  
142 point. Eq. 2 indicates that the side of a drainage divide with a higher  $A_{cr}$  or  $S_{ch}$  can  
143 have a higher erosion rate than the other side, and is more likely to pirate the opposite  
144 drainage basin. Besides, a high erosion coefficient can amplify the drainage basin's  
145 erosion rate.

146 Drainage-divide migration is essentially controlled by the cross-divide difference  
147 in erosion rates and topographic slope (Beeson et al., 2017; Dahlquist et al., 2018;  
148 Chen et al., 2021; Zhou et al., 2022a; Stokes et al., 2023). Furthermore, the  
149 differential uplift should also be considered when using the cross-divide erosion rates  
150 at the channel heads to calculate the erosion difference across the divide, especially in

151 the case of tectonic tilting uplift (Zhou et al., 2022a). The drainage-divide migration  
 152 rate ( $D_{mr}$ ) can be obtained according to the cross-divide difference in erosion rate and  
 153 uplift rate and the slopes across the divide (Zhou et al., 2022a):

$$154 \quad D_{mr} = \frac{\Delta E_{ch} - \Delta U_{ch}}{\tan\alpha + \tan\beta} \quad (3)$$

155 where  $\Delta E_{ch}$  is the difference in erosion rate between the two sides (annotated as  $\alpha$  and  
 156  $\beta$ ) of the drainage divide ( $\Delta E_{ch} = E_{cha} - E_{ch\beta}$ ). The choice of  $\alpha$  or  $\beta$  is arbitrary, and the  
 157 positive direction of the migration rate is assigned from the  $\alpha$  to the  $\beta$  side whereas the  
 158 negative is the opposite.  $\Delta U_{ch}$  is the cross-divide difference in uplift rate ( $\Delta U_{ch} = U_{cha}$   
 159  $- U_{ch\beta}$ ), and  $\tan\alpha$  and  $\tan\beta$  are the average gradients (along the normal-divide  
 160 direction) upslope of the channel head (not including the hilltop part) on the  $\alpha$  side  
 161 and the  $\beta$  side, respectively. Assuming the erosion coefficient ( $K$ ) is the same on both  
 162 sides of a drainage divide, Eqs. 2 and 3 allow us to derive the equation of drainage  
 163 divide's migration rate according to the parameters at the channel-head points:

$$164 \quad D_{mr} = \frac{K[(A_{cr}^m S_{ch}^n)_\alpha - (A_{cr}^m S_{ch}^n)_\beta] - \Delta U_{ch}}{\tan\alpha + \tan\beta} \quad (4)$$

165 If the exact value of  $K$  is unknown, the drainage divide's unilateral erosion rate  
 166 can be used as a substitution:

$$167 \quad D_{mr} = \frac{E_\alpha \left[ 1 - \frac{(A_{cr}^m S_{ch}^n)_\beta}{(A_{cr}^m S_{ch}^n)_\alpha} \right] - \Delta U_{ch}}{\tan\alpha + \tan\beta} \quad (5)$$

168 or:

$$169 \quad D_{mr} = \frac{E_\beta \left[ \frac{(A_{cr}^m S_{ch}^n)_\alpha}{(A_{cr}^m S_{ch}^n)_\beta} - 1 \right] - \Delta U_{ch}}{\tan\alpha + \tan\beta} \quad (6)$$

170  $E_\alpha$  and  $E_\beta$  are the erosion rates of the  $\alpha$  and the  $\beta$  side of the drainage divide,  
 171 respectively, which can be derived through cosmogenic nuclides ( $^{10}\text{Be}$ ) concentration



172 measurements (Beeson et al., 2017; Godard et al., 2019; Hu et al., 2021). The regional  
 173 average erosion rate ( $\bar{E} = \frac{E_\alpha + E_\beta}{2}$ ) can also be used to calculate the migration rate:

$$174 \quad D_{mr} = \frac{2\bar{E} \left[ \frac{(A_{cr}^m S_{ch}^n)_\alpha - (A_{cr}^m S_{ch}^n)_\beta}{(A_{cr}^m S_{ch}^n)_\alpha + (A_{cr}^m S_{ch}^n)_\beta} \right] - \Delta U_{ch}}{\tan\alpha + \tan\beta} \quad (7)$$

175 Based on Eqs. 4-7, the migration rate of drainage divides can be estimated using  
 176 channel-head parameters combined with one of the erosion-related parameters,  
 177 erosion coefficient ( $K$ ), erosion rate at one side of a drainage divide ( $E_\alpha$  or  $E_\beta$ ), or  
 178 regional average erosion rate ( $\bar{E}$ ).

179

## 180 2.2 Channel-head-segment method

181 A channel-head segment is the channel segment just below the channel head  
 182 (Zhou et al., 2022a). Zhou et al. (2022a) developed a method based on the cross-  
 183 divide  $\chi$  contrast of channel-head segments to calculate the migration rate of drainage  
 184 divides. The essence of the method is the cross-divide comparison of the channel-  
 185 head segments' normalized channel steepness ( $k_{sn}$ ) values.  $k_{sn}$  is a widely used index  
 186 (Whipple et al., 1999; Wobus et al., 2006; Hilley and Arrowsmith, 2008; Kirby and  
 187 Whipple, 2012) that is quantitatively related to  $E$  and  $K$  ( $k_{sn} = \left(\frac{E}{K}\right)^{\frac{1}{n}}$ ).  $\chi$  is an integral  
 188 function ( $\chi = \int_{x_b}^x \left(\frac{A_0}{A(x)}\right)^{\frac{m}{n}} dx$ ) of a channel's upstream area ( $A$ ) to horizontal distance  
 189 ( $x$ ) (Royden et al., 2000; Perron and Royden, 2012), and  $A_0$  is an arbitrary scaling area  
 190 to make the integrand dimensionless.

191 In the method of Zhou et al. (2022a), the location of channel heads cannot be  
 192 accurately identified, because it is limited by the resolution of DEM. Therefore, an

193 empirical value of  $A_{cr} = 10^5 \text{ m}^2$  was used in the calculation. Benefiting from the high-  
 194 resolution DEM in this study, we improve the method in Zhou et al. (2022a) and use  
 195 the real location of channel heads to calculate the migration rate. When the regional  
 196 erosion coefficient ( $K$ ) is known and unchanged in the vicinity of the drainage divide,  
 197 the drainage-divide migration rate can be estimated by the following equation:

$$198 \quad D_{mr} = \frac{K[k_{sn(\alpha)}^n - k_{sn(\beta)}^n] - \Delta U_{ch}}{\tan\alpha + \tan\beta} = \frac{K \left\{ \left[ \frac{(z_{ch} - z_b)_\alpha}{\chi_\alpha} \right]^n - \left[ \frac{(z_{ch} - z_b)_\beta}{\chi_\beta} \right]^n \right\} - \Delta U_{ch}}{\tan\alpha + \tan\beta} \quad (8)$$

199 where  $z_{ch}$  is the elevation of the channel head,  $z_b$  is the elevation of catchment outlet  
 200 (at the top part of the channel to make the elevation- $\chi$  profiles quasi-linear between  
 201 the channel head and the outlet), and subscripts  $\alpha$  and  $\beta$  denote the two rivers across a  
 202 divide. The detailed derivation of Eq. 8 is in Supplementary Materials. The drainage  
 203 divide's unilateral erosion rate ( $E_\alpha$  or  $E_\beta$ ) can also be used as a substitution for the  $K$   
 204 value:

$$205 \quad D_{mr} = \frac{E_\alpha \left\{ 1 - \left( \frac{\chi_\alpha}{\chi_\beta} \right)^n \left[ \frac{(z_{ch} - z_b)_\alpha}{(z_{ch} - z_b)_\beta} \right]^{-n} \right\} - \Delta U_{ch}}{\tan\alpha + \tan\beta} \quad (9)$$

206 or:

$$207 \quad D_{mr} = \frac{E_\beta \left\{ \left( \frac{\chi_\alpha}{\chi_\beta} \right)^{-n} \left[ \frac{(z_{ch} - z_b)_\alpha}{(z_{ch} - z_b)_\beta} \right]^n - 1 \right\} - \Delta U_{ch}}{\tan\alpha + \tan\beta} \quad (10)$$

208 Alternatively, one can use the regional average erosion rate ( $\bar{E}$ ) to calculate the  
 209 migration rate:

$$210 \quad D_{mr} = \frac{2\bar{E} \left\{ \frac{\left[ \frac{(z_{ch} - z_b)_\alpha}{(z_{ch} - z_b)_\beta} \right]^n - \left( \frac{\chi_\alpha}{\chi_\beta} \right)^n}{\left[ \frac{(z_{ch} - z_b)_\alpha}{(z_{ch} - z_b)_\beta} \right]^n + \left( \frac{\chi_\alpha}{\chi_\beta} \right)^n} \right\} - \Delta U_{ch}}{\tan\alpha + \tan\beta} \quad (11)$$

211 Based on Eqs. 8-11, the drainage-divide migration rate can be estimated using the  $\chi$

212 values of high-base-level channel segments combined with one of the erosion-related  
213 parameters, erosion coefficient ( $K$ ), erosion rate at one side of a drainage divide ( $E_\alpha$  or  
214  $E_\beta$ ), or regional average erosion rate ( $\bar{E}$ ).

215

## 216 **2.3 Parameter extraction**

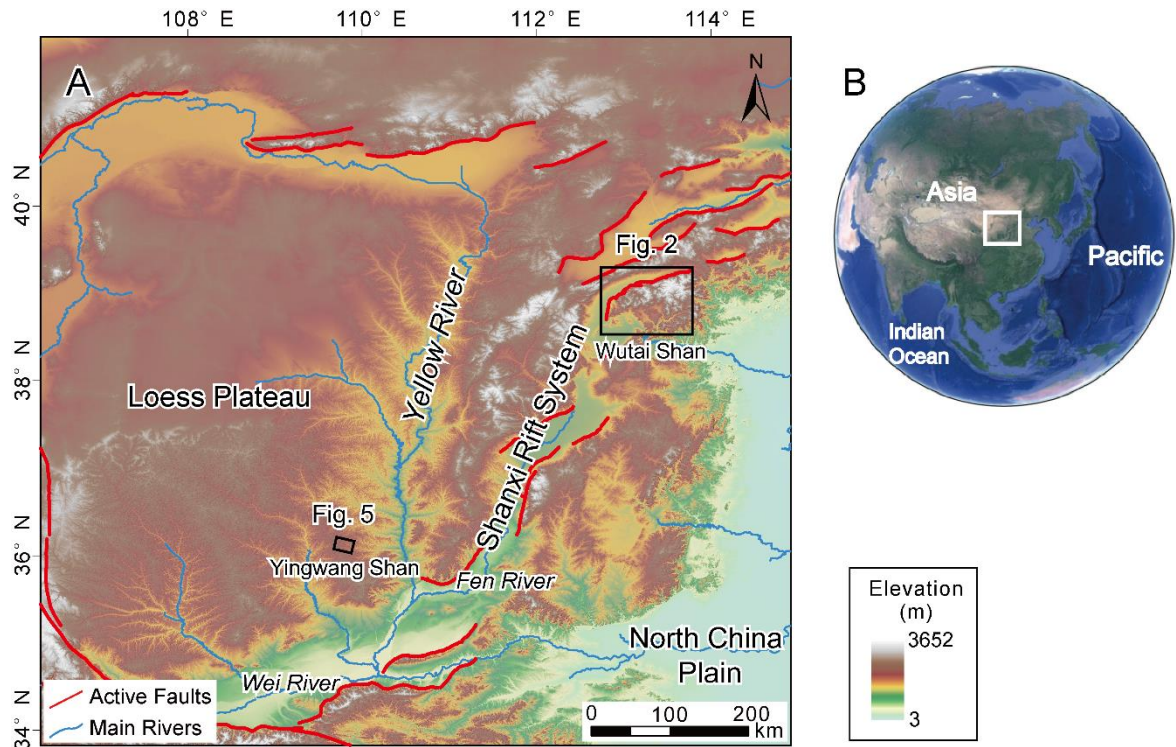
217 In this study, we apply the erosion coefficient ( $K$ ) related equations (Eqs. 4 & 8)  
218 to two natural examples in North China, the Wutai Shan in the Shanxi Rift and the  
219 Yingwang Shan in the Loess Plateau, to demonstrate how to calculate the drainage-  
220 divide migration rates (Fig. 1). We calculated the  $K$ , according to the equation,  $K =$   
221  $\frac{E}{k_{sn}^n}$ , the erosion rate obtained by chronological methods, the  $k_{sn}$ , and the assumed  
222 slope exponent ( $n = 1$ ). The  $k_{sn}$  is calculated based on  $S$  and  $A$  ( $k_{sn} = SA^{\frac{m}{n}}$ ) extracted  
223 from ALOS DEM (downloaded from <https://search.asf.alaska.edu/>) using  
224 TopoToolbox (Schwanghart and Scherler, 2014), and the interpolation uses the  
225 Kriging method on ArcGIS (Fig. 2). We use a small four-rotor Unmanned Aerial  
226 Vehicle (UAV), the DJI Phantom 4, to acquire stereo images of the areas. Based on  
227 the Structure-from-Motion (SfM) method and PhotoScan software, we obtained the  
228 DEMs with a spatial resolution of 0.67 m in the Wutai Shan and 0.84 m in the  
229 Yingwang Shan (can be download from <https://doi.org/10.5069/G98C9TGT>). Both  
230 regions are semi-arid, and the vegetation is dominated by shrubs. We did not compare  
231 the elevations to the standard GPS points, which may bring errors on the elevations.

232 Based on the high-resolution topography data, we first extract river channels and

233 drainage divide, using a single-flow-direction algorithm (D8). Then we extract the  
234 relevant parameters, and calculate the drainage-divide migration rate. Data analysis  
235 including slope-area plots,  $\chi$ -plots, river's long profiles and topographic swath  
236 profiles, are based on the Matlab toolbox TAK (Forte and Whipple, 2019) and  
237 TopoToolbox (Schwanghart and Scherler, 2014). According to the breaking point of  
238 the slope-area regression line, we obtain the value of the critical upstream drainage  
239 area ( $A_{cr}$ ) of each river channel (Duvall et al., 2004). According to these values, we  
240 mark the position (and its elevation,  $z_{ch}$ ) of the channel heads on the  $\chi$ -plots and the  
241 topography map. An elevation of the catchment outlet ( $z_b$ ) can be assigned at the top  
242 part of the channel to make the elevation- $\chi$  profiles quasi-linear between the channel  
243 head and the outlet. The slope of the channel head ( $S_{ch}$ ) is calculated, according to the  
244 100 m long channel on the river's long profiles around the channel head (50 m  
245 upstream and downstream). Topographic gradient ( $\tan\alpha$  or  $\tan\beta$ ) is calculated through  
246 the average slope (in the normal-divide direction) of the hillslope segment (not  
247 including the hilltop part, because of its lower gradient). The cross-divide uplift  
248 difference in the channel-head points ( $\Delta U_{ch}$ ) is estimated according to the location of  
249 the each channel head and the tectonic uplift trend.

250

251 **3. Applications to natural cases**



252  
253 **Figure 1.** Locations and tectonic background of the two nature cases in North China.

254 The figure is modified from Fig. 7 in Shi et al. (2021). (A) Red lines represent the  
255 main active faults. Black rectangles show the locations of the two nature cases. Red  
256 curve denotes active fault, sourced from <https://www.activefault-datacenter.cn/>. The  
257 topography data (ALOS DEM) is downloaded from the Alaska Satellite Facility  
258 (ASF) Data Search (<https://search.asf.alaska.edu/>). (B) The satellite image downloaded  
259 from Google Earth. White rectangles show the location of Panel A.

260

261 **3.1 Wutai Shan**

262 The Wutai Shan is a tilted fault block on the shoulder of the Shanxi Rift System  
263 located in the central North China craton (Fig. 1) (Xu et al., 1993; Su et al., 2021).

264 The tilting uplift of the Wutai Shan is controlled by the Northern Wutai Shan fault,  
265 and there is no active fault along the south edge of the Wutai Shan horst (Fig. 2). The  
266 bedrock of the Wutai Shan area consists mainly of metamorphic and igneous  
267 basement rocks (Clinkscales et al., 2020) and there is no obvious variation in rock  
268 erodibility and precipitation in this area (Fig. S2 & S3). Zhou et al. (2022b) reveal that  
269 the Wutai Shan drainage divide is migrating northwestward due to the tilting uplift  
270 and predicts the drainage divide will move ~10 km to the northwest to achieve a  
271 steady state if all geological conditions remain. Geomorphic evidence also exhibits a  
272 northwestward migration of the drainage divide (Fig. 3). The plan and satellite views  
273 show several abnormally high junction angles around the Wutai Shan drainage divide,  
274 which indicate that the tributaries formerly part of the northern drainage have become  
275 part of the southern drainage (Fig. 3A&B). The  $\chi$ -plots analysis shows the southern  
276 side of the drainage divide has steeper channels, higher  $k_{sn}$ , and lower  $\chi$ . The  $\chi$ -plots  
277 of paired rivers illustrate obvious characteristics of shrinking-expanding and captured-  
278 beheaded rivers (Fig. 3C).

279 To derive the erosion coefficient of the Wutai Shan area, we calculate the  
280 channel steepness ( $k_{sn}$ ) of this region, assuming  $n = 1$  and  $m = 0.45$  (Wobus et al.,  
281 2006; DiBiase et al., 2010; Perron and Royden, 2012; Wang et al., 2021). We then use  
282 the Kriging interpolation method to generate the  $k_{sn}$  distribution map (Fig. 2B). In  
283 addition, results under the assumptions of  $m = 0.35$  and  $0.55$ , respectively, are shown  
284 in Supplementary Materials (Fig. S4). The average  $k_{sn}$  value of the upthrown side near  
285 the Northern Wutai Shan fault is  $\sim 80 \text{ m}^{0.9}$  (Fig. 2D). Middleton et al. (2017) showed

286 that the Quaternary throw rates of the Northern Wutai Shan fault are 0.8-1.6 mm/yr.  
287 Clinkscales et al. (2020) showed, using low-temperature thermochronology, that the  
288 time-averaged long-term throw rates in the late Cenozoic is about 0.25 mm/yr, and  
289 there is an accelerated activity in the Wutai Shan area. According to these studies, we  
290 assume a  $0.50 \pm 0.25$  mm/yr uplift/erosion rate in the northern margin of the Wutai  
291 Shan (in the footwall of the Northern Wutai Shan fault). Combining with the equation,  
292  $K = \frac{E}{k_{sn}n}$ , and following the approach of previous studies (Kirby and Whipple, 2001;  
293 Kirkpatrick et al., 2020; Ma et al., 2020), the erosion coefficient ( $K$ ) is calculated to  
294 be  $(6.25 \pm 3.13) \times 10^{-6} \text{ m}^{0.1} \text{ yr}^{-1}$  in this area. Because there is no obvious variation in  
295 rock erodibility and precipitation in this area (Figs. S2 & S3), we use this value as the  
296 erosion coefficient ( $K$ ) of the Wutai Shan area.

297 We then apply the two new methods (Eqs. 4 & 8) to calculate the migration rate  
298 of the drainage divide in the Wutai Shan. We first choose three pairs of rivers (Fig.  
299 4A) and acquire their slope-area plots (Figs. 4B, E, H) and the  $\chi$ -plots (Figs. 4C, F, I).  
300 According to the breaking point of the slope-area regression line (Duvall et al., 2004)  
301 (Figs. 4B, E, H), we obtain the values of the critical upstream drainage area ( $A_{cr}$ ).  
302 According to these values, we separate hillslope and channel areas and mark the  
303 position of the channel heads on the  $\chi$ -plots and the topography map (Fig. 4A). For  
304 the  $\chi$ -plots (Figs. 4C, F, I), we obtain the elevations of channel heads ( $z_{ch}$ ) and  $\chi$  values  
305 based on the coordinate of the channel-head points. According to the location of the  
306 channel heads on the river's long profiles, we calculate the channel-head gradient  
307 ( $S_{ch}$ ). Topographic gradient ( $\tan\alpha$  or  $\tan\beta$ ) is calculated through the average slope (in

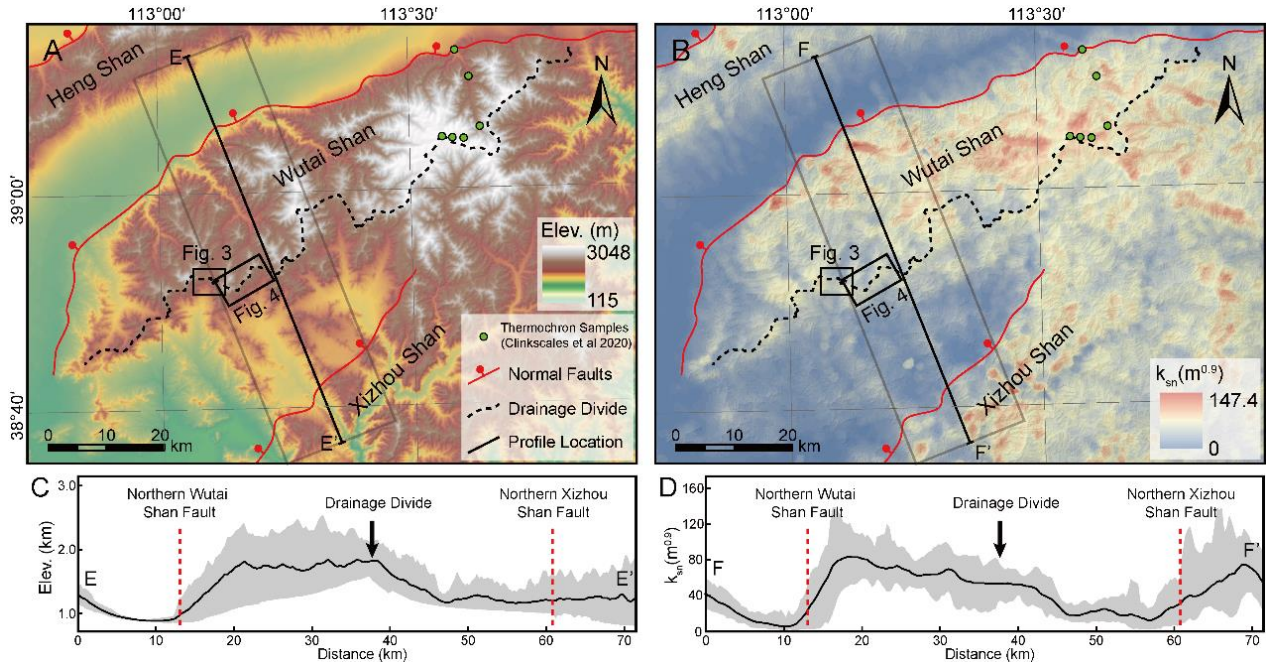
308 the normal-divide direction) of the hillslope segment (not including the hilltop part,  
309 Figs. 4D, G, J).

310 According to the previous studies (Middleton et al., 2017; Clinkscales et al.,  
311 2020) and the  $k_{sn}$  distribution (Fig. 2D), we assume the rock uplift rate decreases  
312 linearly from 0.5 to 0 mm/yr from northwest to southeast of the Wutai Shan horst  
313 (~40 km wide). Then we can obtain that the cross-divide uplift difference in the  
314 channel-head points ( $\Delta U_{ch}$ ) (the distance perpendicular to the direction of the  
315 boundary fault is ~600 m) is ~0.008 mm/yr. After determining these parameters, we  
316 adopt the channel-head-point (Eq. 4) and channel-head-segment (Eq. 8) methods,  
317 respectively, to calculate the migration rates. The required data for calculation and the  
318 migration rates are shown in Table 1. The calculated results for  $m/n = 0.35$  and  $0.55$ ,  
319 respectively, are shown in Supplementary Materials (Table S1). The migration rates  
320 are higher when  $m/n = 0.35$  and lower when  $m/n = 0.55$ , which indicates the  $m/n$  value  
321 is sensitive to the result.

322 The rivers have different characteristics on both sides of the drainage divide, as  
323 illustrated on their slope-area plots (Figs. 4B, E, H) and the  $\chi$ -plots (Figs. 4C, F, I).  
324 For the first site (Fig. 4D), the migration rates calculated by the channel-head-point  
325 and channel-head-segment methods are 0.21 mm/yr and 0.26 mm/yr, respectively. For  
326 the second site (Fig. 4G), the migration rates are 0.23 mm/yr and 0.27 mm/yr,  
327 respectively. For the third site (Fig. 4J), 0.21 mm/yr and 0.22 mm/yr, respectively. The  
328 drainage divides of all three points are migrating northwestward, which is consistent  
329 with the previous result inferred by the cross-divide contrast of slopes in this area

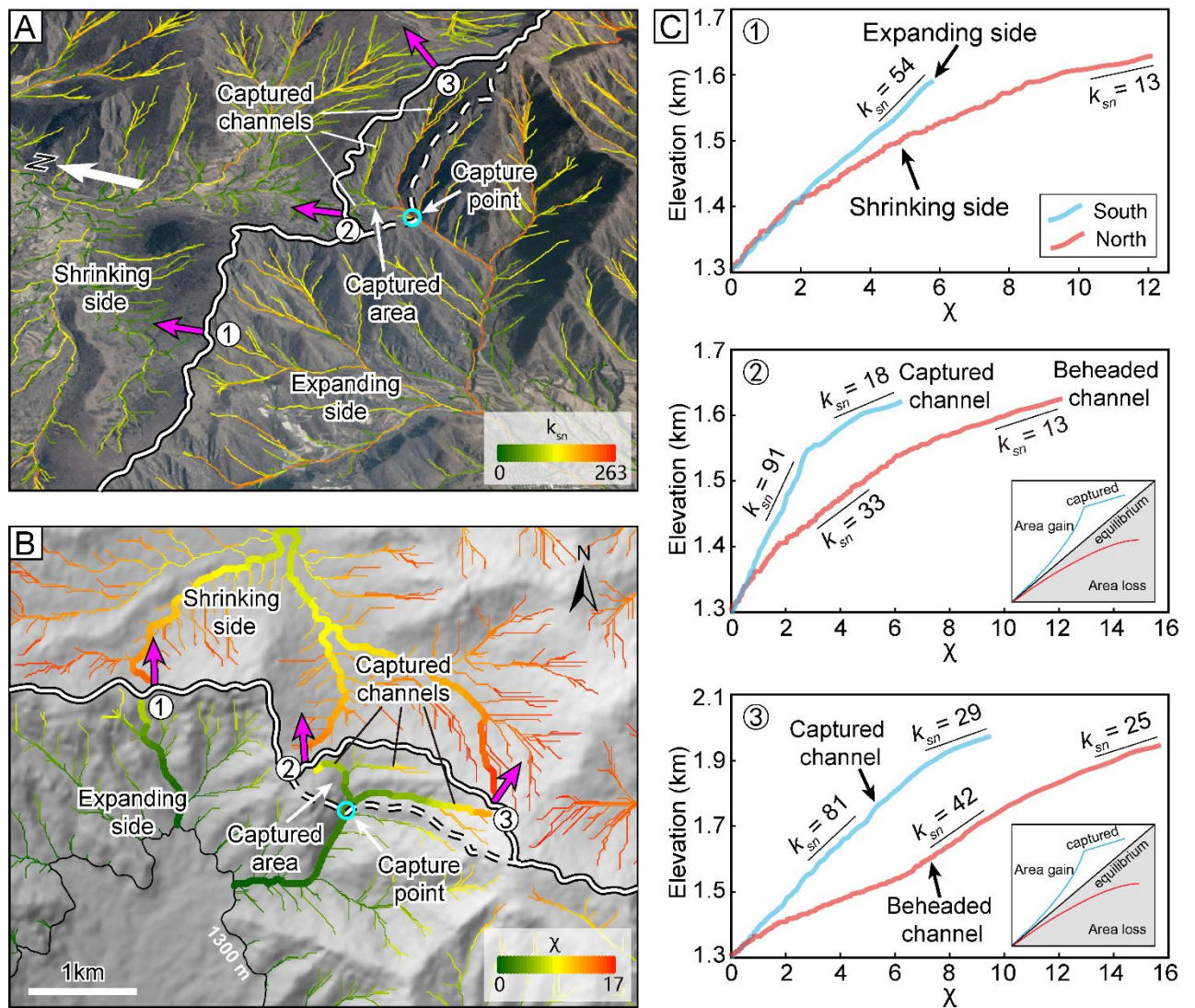


330 (Zhou et al., 2022b). Furthermore, the migration rates calculated by the two methods  
 331 are comparable in all three sites.  
 332



333  
 334 **Figure 2.** Topography (A) and normalized channel steepness ( $k_{sn}$ ) (B) distribution of  
 335 the Wutai Shan horst and surrounding area in the Shanxi Rift System. The black  
 336 dashed line shows the location of the main drainage divide. Red lines show the main  
 337 active faults. The black lines show the location of profiles E-E' and F-F'. Black  
 338 rectangles show the area of Fig. 3B & 4A. Gray boxes show the area of the swath  
 339 profiles in Panels C and D. Green dots denote the locations of the low-temperature  
 340 thermochronology samples in Clinkscales et al. (2020). The  $k_{sn}$  is calculated based on  
 341  $S$  and  $A$  extracted from ALOS DEM ( $k_{sn} = SA^{\frac{m}{n}}$ ) and a uniform  $m/n$  (0.45) using  
 342 TopoToolbox (Schwanghart and Scherler, 2014), and the interpolation uses the  
 343 Kriging method on ArcGIS. (C) Topography swath profile along E-E'. See location in  
 344 Panel A. (D)  $k_{sn}$  swath profile along F-F'. See location in Panel B. The swath profiles

345 are extracted using TopoToolbox (Schwanghart and Scherler, 2014). The red dashed  
 346 lines show the location of the main active normal faults, and the black arrow shows  
 347 the location of the main drainage divide. Both swath profiles are 20 km wide (10 km  
 348 on each side).  
 349

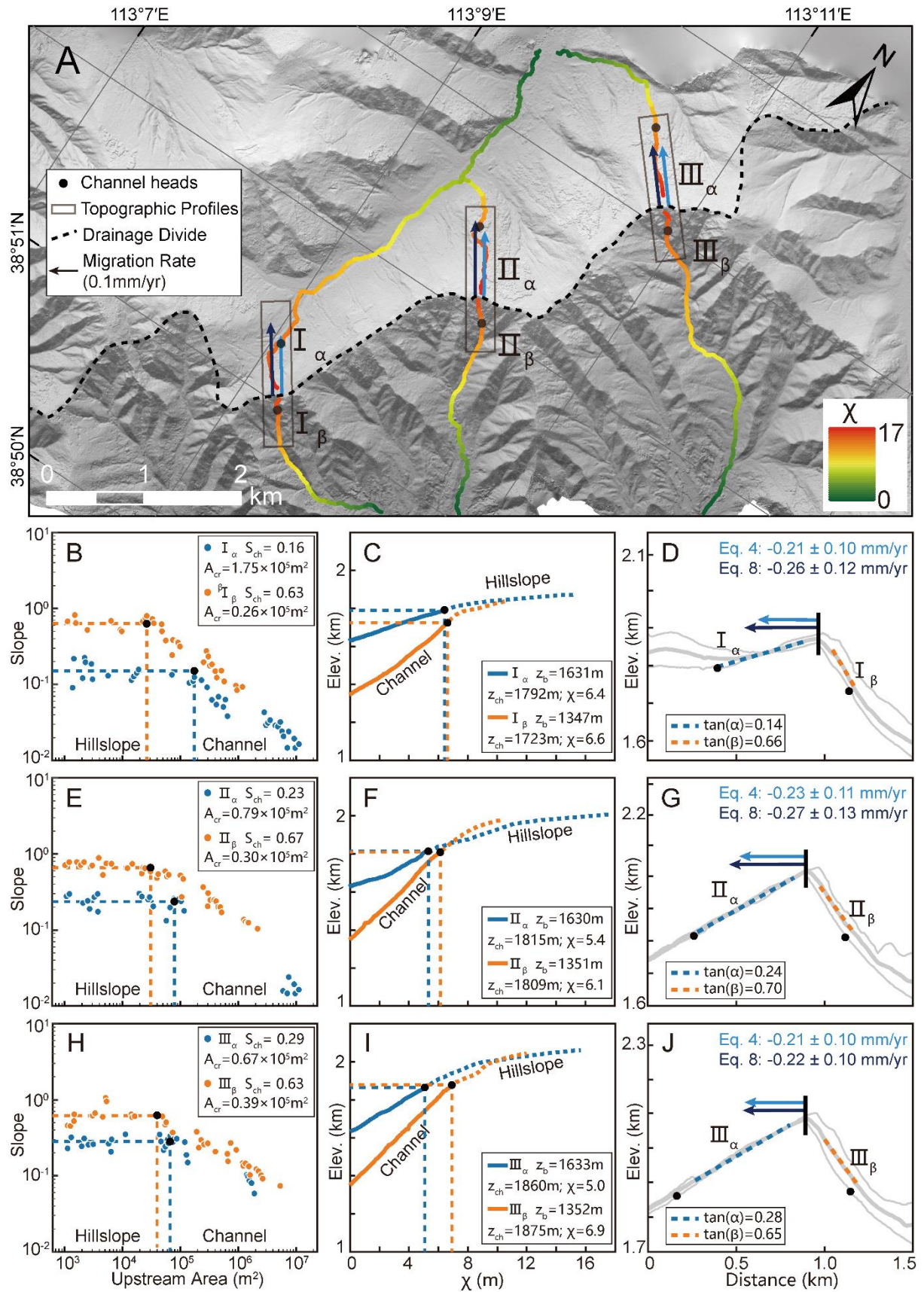


350  
 351 **Figure 3.** Perspective views and  $\chi$  map of the drainage divide in the Wutai Shan (see  
 352 Fig. 2 for location). (A) Perspective views of a captured area and the channels mapped  
 353 with  $k_{sn}$ . The south side of the drainage divide has steeper channels and higher  $k_{sn}$  than  
 354 the north side. Magenta arrows show drainage divide migration directions. The

355 satellite image is from Google Earth. (B)  $\chi$  map of this area with the outlet elevation  
356 of 1300 m. The south side of the drainage divide has lower  $\chi$  values than the north  
357 side. It should be noted that the catchment outlet at the north side of the drainage  
358 basins (the 1300 m contour) is out of the map. The  $\chi$ -plots of the rivers in bold lines  
359 are shown in Panel C. (C)  $\chi$ -plots of the three paired rivers in Panel B. The blue and  
360 red curves correspond to the rivers on the south and north sides, respectively. The  $\chi$ -  
361 plot of River 1 is steeper on the south side, indicating that the river on the south side  
362 is expanding and the river on the north side is shrinking. The  $\chi$ -plots of Rivers 2 and 3  
363 in the captured area show obvious characteristics of the captured and beheaded rivers.  
364 The  $\chi$ -plot is extracted using TAK ([Forte and Whipple, 2019](#)) and TopoToolbox  
365 ([Schwanghart and Scherler, 2014](#)).

366





367

368 **Figure 4.** Analytical results of the Wutai Shan drainage divide. (A) High-resolution

369 hill-shade map (0.67 m spatial resolution) of the Wutai Shan. The black dashed line

370 shows the location of the main drainage divide. Colored lines show the three pairs of  
371 selected channels used for analysis. The black dots are the channel heads. Black  
372 rectangles show the location of the cross-divide topography swath profiles. The black  
373 arrows show the direction of drainage-divide migration (**B, E, H**) Slope-area plots of  
374 the three pairs of selected channels. The blue and orange dots are the slope-area plots  
375 of the north ( $\alpha$ ) and south ( $\beta$ ) sides of the drainage divide respectively. The black dots  
376 represent the channel heads. (**C, F, I**)  $\chi$ -plots of the selected channels. The blue and  
377 orange lines are the  $\chi$ -plots of the north ( $\alpha$ ) and south ( $\beta$ ) sides of the drainage divide  
378 respectively. The black dots represent the channel heads. (**D, G, J**) Cross-divide  
379 topography swath profiles with the drainage-divide migration rates. The locations of  
380 the profiles are in Panel A. The light and dark blue arrows are the drainage-divide  
381 migration rates calculated by the channel-head-point (Eq. 4) and channel-head-  
382 segment (Eq. 8) methods respectively.

383

### 384 **3.2 Yingwang Shan**

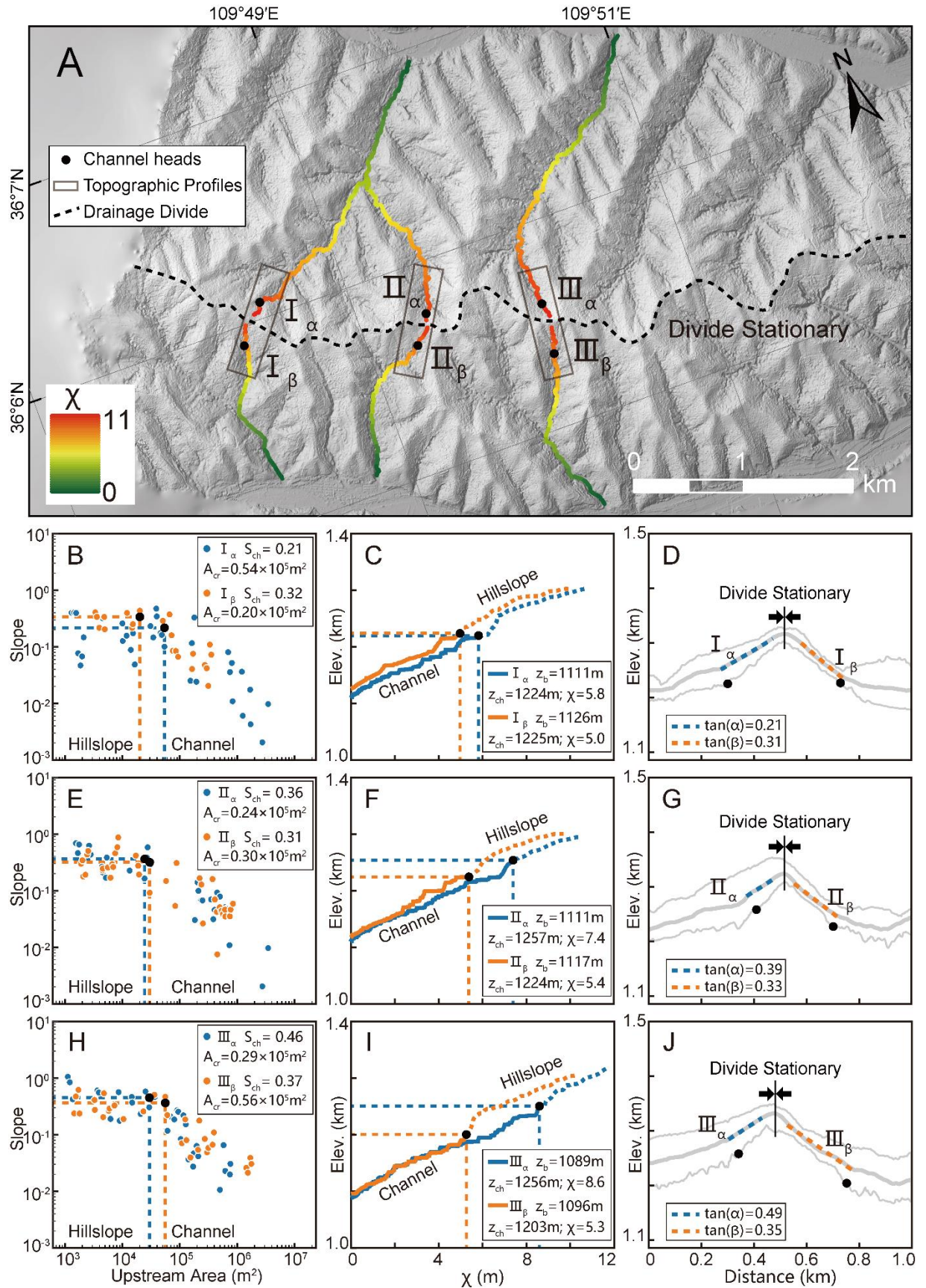
385 The Loess Plateau is hosted by the tectonically stable Ordos Block of the North  
386 China craton (Yin, 2010; Su et al., 2021). Over the past 2.6 million years, it has  
387 accumulated tens to hundreds of meters of eolian sediments (Yan et al., 2014),  
388 draping preexisting topography (Xiong et al., 2014). There is no active fault and little  
389 to no variation in rock erodibility and precipitation within the area (Shi et al., 2020;  
390 Zhou et al., 2022b).

391 We apply the two methods to Yingwang Shan of Loess Plateau to calculate the  
392 drainage-divide migration rate. Similar to the Wutai Shan site, we obtain the slope-  
393 area plots (Figs. 5 B, E, H), the  $\chi$ -plots (Figs. 5 C, F, I), and extract the values of  $A_{cr}$ ,  
394  $S_{ch}$ ,  $z_b$ ,  $z_{ch}$ ,  $\gamma$ ,  $\tan\alpha$  and  $\tan\beta$  of the rivers. The rate of soil erosion in the study area is  
395 about  $500 \text{ t}\cdot\text{km}^{-2}\cdot\text{yr}^{-1}$  according to the distribution of silt discharge (Fu, 1989).  
396 Combining with the assumption of the density of loess,  $1.65 \text{ t}\cdot\text{m}^{-3}$ , the present-day  
397 erosion rate in the study area is calculated to be  $0.3 \text{ mm}\cdot\text{yr}^{-1}$ . Because there is no  
398 obvious unequal uplift in this region, we assign that  $\Delta U_{ch}$  is zero. We also assume  $n =$   
399  $1$  and  $m = 0.45$  in the calculation (Wobus et al., 2006; DiBiase et al., 2010; Perron and  
400 Royden, 2012; Wang et al., 2021). Then, we use the methods of channel-head  
401 parameters (Eq. 7) and channel segments (Eq. 11) to calculate the drainage-divide  
402 migration rates. The required data for calculation and the migration rates are shown in  
403 Table 1.

404 All results of the three points show that the drainage-divide migration rate here is  
405 close to zero, no matter which method is used in the calculation. The results show that  
406 the drainage divide of the study site is in topographical equilibrium, which is  
407 consistent with the inference in previous studies (Willett et al., 2014, Zhou et al.,  
408 2022b).

409





410

411 **Figure 5.** Analytical results of the Yingwang Shan in the Loess Plateau. (A) High-

412 resolution hill-shade map (0.84 m spatial resolution). The black dotted line shows the  
413 location of the main drainage divide. Colored lines show the three pairs of selected  
414 channels used for analysis. The black dots represent the channel heads. Black  
415 rectangles show the location of the cross-divide topography swath profiles. **(B, E, H)**  
416 Slope-area plots of the three pairs of selected channels. The blue and orange dots are  
417 the data of the north ( $\alpha$ ) and south ( $\beta$ ) sides of the drainage divide respectively. The  
418 black dots represent the channel heads. **(C, F, I)**  $\chi$ -plots of the selected channels. The  
419 blue and orange lines are the  $\chi$ -plots of the north ( $\alpha$ ) and south ( $\beta$ ) sides of the  
420 drainage divide respectively. The black dots represent the channel heads. **(D, G, J)**  
421 The cross-divide topography swath profiles. The locations of the swath profiles are in  
422 Panel A.  
423



**Table 1.** Channel parameters and migration rates of drainage divides in two field cases.

Natural Cases	No.	$A_{cr}$ ( $\times 10^5 \text{m}^2$ )	$S_{ch}$	$z_b$ (m)	$z_{ch}$ (m)	$\chi$	$\tan\alpha$	$\tan\beta$	$\Delta U_{ch}$ (mm/yr)	$D_{mr}$ (mm/yr) (Channel-head-point method)	$D_{mr}$ (mm/yr) (Channel-head-segment method)
Wutai Shan	Fig. 4 I $\alpha$	1.75	0.16	1631	1792	6.4	0.14	0.66	$\sim 0.008$	$-0.21 \pm 0.10$	$-0.26 \pm 0.12$
	Fig. 4 I $\beta$	0.26	0.63	1347	1723	6.6					
	Fig. 4 II $\alpha$	0.79	0.23	1630	1815	5.4	0.24	0.70	$\sim 0.008$	$-0.23 \pm 0.11$	$-0.27 \pm 0.13$
	Fig. 4 II $\beta$	0.30	0.67	1351	1809	6.1					
	Fig. 4 III $\alpha$	0.67	0.29	1633	1860	5.0	0.28	0.65	$\sim 0.008$	$-0.21 \pm 0.10$	$-0.22 \pm 0.10$
Fig. 4 III $\beta$	0.39	0.63	1352	1875	6.9						
Yingwang Shan	Fig. 5 I $\alpha$	0.54	0.21	1111	1224	5.8	0.21	0.31	0	$\sim 0.03$	$\sim -0.01$
	Fig. 5 I $\beta$	0.20	0.32	1126	1225	5.0					
	Fig. 5 II $\alpha$	0.24	0.36	1111	1257	7.4	0.39	0.33	0	$\sim 0.02$	$\sim -0.01$
	Fig. 5 II $\beta$	0.30	0.31	1117	1224	5.4					
	Fig. 5 III $\alpha$	0.29	0.46	1089	1256	8.6	0.49	0.35	0	$\sim 0.02$	$\sim -0.01$
Fig. 5 III $\beta$	0.56	0.37	1096	1203	5.3						

## 426 **4. Discussion**

### 427 **4.1 Location of channel heads**

428 Willett et al. (2014) pioneered the use of cross-divide  $\chi$  contrast to gauge the  
429 horizontal motion of drainage divides. According to their method, drainage divides  
430 are predicted to move toward the side with a higher  $\chi$  value to achieve geomorphic  
431 equilibrium. However, in a region with spatially variable uplift rates, lithology, or  
432 precipitation,  $\chi$  contrast may fail to reflect the drainage-divide migration (Willett et  
433 al., 2014; Whipple et al., 2017; Forte and Whipple, 2018; Wu et al., 2022; Zhou and  
434 Tan, 2023). In a tectonically active area, the cross-divide  $\chi$  contrast can only be used  
435 in a small area where rock type, precipitation, and uplift rate are nearly uniform  
436 (Willett et al., 2014). Combining the advantages of the  $\chi$  and Gilbert metrics methods,  
437 Zhou et al. (2022a) proposed to use the  $\chi$  contrast with a high base level to calculate  
438 the  $k_{sn}$  values at the channel heads on both sides of a drainage divide, and quantified  
439 the migration rate of drainage divides at the eastern margin of Tibet.

440 To reduce the cross-divide difference in uplift rate, precipitation, and rock  
441 strength, the Gilbert metrics or  $\chi$ -comparison method in Zhou et al. (2022a) should  
442 compare the parameters of points (slope, relief, elevation, and  $k_{sn}$ ) on both sides of the  
443 divide as closely as possible. As the hillslope area (above the channel head) does not  
444 follow Eq. 1 (Stock and Dietrich, 2006; Stark, 2010; Braun et al., 2018; Dahlquist et  
445 al., 2018), the channel heads are the closest point to the divide, following Eq. 1.  
446 Channel heads, therefore, are suitable for measuring the drainage-divide stability with

447 parameters of the upstream drainage area and channel gradient (Forte and Whipple,  
448 2018; Zhou et al., 2022a). However, limited by the resolution of DEM, the location of  
449 the channel heads cannot always be accurately identified. The channel head  
450 parameters for calculating the migration rates are usually based on empirical values  
451 (both sides are the same value) in previous studies (e.g.,  $A_{cr} = 10^5 \text{ m}^2$  in Zhou et al.  
452 (2022a)), which may induce uncertainties.

453 In this study, we advocate the use of high-resolution DEM to determine a more  
454 accurate position and related parameters of the channel head. The use of UAVs to  
455 obtain the local DEM has become highly efficient. We advance the theory to calculate  
456 the drainage-divide migration rate based on the measured channel-head parameters.  
457 With the help of the aerial photography of UAVs and the SfM techniques, it is  
458 possible to obtain the high-resolution topography data of drainage divides (Figs. 4A &  
459 5A) and get the required parameters through topography analysis. The key parameters  
460 includes the exact locations (usually have different  $A_{cr}$  across the divides) and the  
461 gradients of the channel heads ( $S_{cr}$ ), which could improve the quantitative research on  
462 the drainage-divide migration. Furthermore, the method provides a new avenue to  
463 combine with catchment-wide  $^{10}\text{Be}$  erosion rate or low-temperature  
464 thermochronology data to calculate the migration rate, which has great potential for  
465 application in places where some variables are hard to be constrained.

466

## 467 **4.2 Cross-divide difference in the uplift rate of the channel heads**

468 Although the channel heads across the divide are very close on the spatial scale of  
469 an orogenic belt, differential uplift between the channel heads ( $\Delta U_{ch}$ ) could still exist,  
470 especially in a tilting horst, such as the Wutai Shan. The cross-divide difference in  
471 uplift rate could impact the calculation of the migration rate of drainage divides (Zhou  
472 et al., 2022a).

473 In this study, we quantify the influence of the cross-divide difference in rock  
474 uplift rate ( $\Delta U_{ch}$ ) on the calculation of the migration rate of drainage divides at the  
475 Wutai Shan, benefiting from the available tectonic and chronological research  
476 (Clinkscales et al., 2020) and the newly obtained high-resolution topographic data. In  
477 the Wutai Shan horst,  $\Delta U_{ch}$  across the drainage divide is  $\sim 0.008$  mm/yr. We estimate  
478 the influence of  $\Delta U_{ch}$  on the drainage-divide migration rate in this case study, which  
479 can reduce the error theoretically. If  $\Delta U_{ch}$  is ignored, the drainage-divide migration  
480 rate would decrease by  $\sim 4\%$  in the Wutai Shan case. Although  $\sim 4\%$  seems to be  
481 negligible, such a ratio will increase if the mountain belt is narrower, the tilting uplift  
482 is stronger, or the divide is closer to the steady state (i.e., the migration rate is lower)  
483 (Whipple et al., 2017; Ye et al., 2022). In other words, the differential uplift may play  
484 a significant influence on the measurement of drainage-divide stability in some  
485 situations. If we consider an extreme example where the main drainage divide of a  
486 tilting mountain range (relatively narrow in width) is at a steady state, the gradient,  
487 relief, and elevation of the channel heads (collectively called “Gilbert metrics”) (Forte  
488 and Whipple, 2018) will show a systematic cross-divide difference in theory. In this

489 case, the drainage divide would be considered unstable if  $\Delta U_{ch}$  were neglected.  
490 Therefore, this study highlights that  $\Delta U_{ch}$  should be taken into account, either in a  
491 qualitative or a quantitative evaluation of the stability of drainage divides using the  
492 parameters on the channel heads.

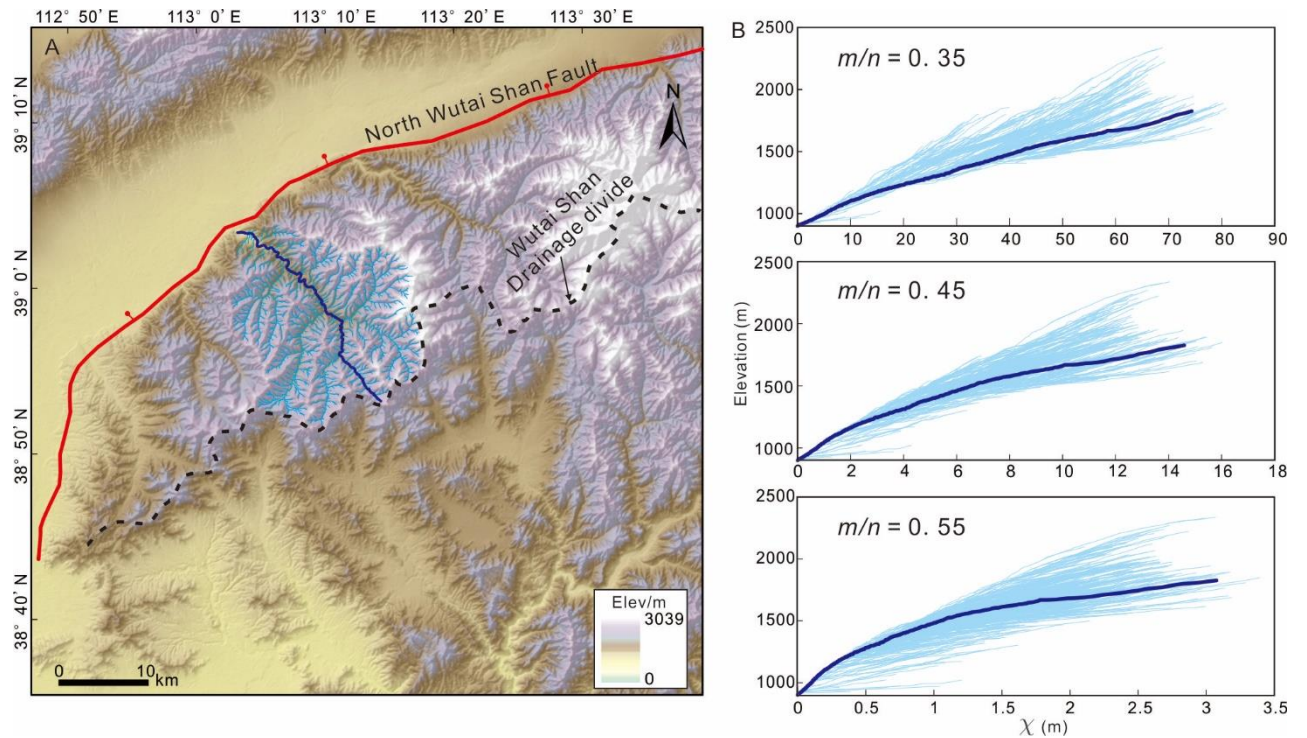
493

### 494 **4.3 Limitations and uncertainties**

495 This study develops the method to calculate the drainage-divide migration rate  
496 based on the measured channel-head parameters. However, uncertainties still exist  
497 because of the limitations of this technique. First, we assume the erosion coefficient  
498 ( $K$ ) is the same on both sides of a drainage divide in the derivation of the equations. If  
499 there are differences in rock erodibility or precipitation across the divide, uncertainties  
500 should exist in the results. Second, the calculation of migration rate is based on the  
501 erosion rates at the channel area in this study. However, the occurrence of drainage-  
502 divide migration is directly driven by the differential erosion of the hillslope area  
503 across the divide, mainly via the processes including landslide, collapse, and diffusion  
504 (Stock and Dietrich, 2006; Stark, 2010; Braun et al., 2018; Dahlquist et al., 2018).  
505 Such discontinuous processes in the hillslope area make it challenging to constrain  
506 erosion rates over such short timescales. Over a relatively longer period (i.e., spanning  
507 multiple seismic and climatic cycles), the erosion rate at the channel head area in this  
508 study can be comparable with that at the hillslope area (Hurst et al., 2012; Godard et  
509 al., 2020).

510 The accuracy of the data and parameters can also impact the reliability of the

511 results. First, we use the uniform values of  $n = 1$  and  $m/n = 0.45$  in the two natural  
512 cases to calculate the migration rate, because it is the best choice to align tributaries  
513 with the main stem on the  $\chi$ -plots in a drainage basin at the northern Wutai Shan (Fig.  
514 6) (Perron and Royden, 2012). If the actual values deviate from the assumption, errors  
515 would be introduced into the results. For this reason, we have added the cases of  $m/n$   
516  $= 0.35$  and  $0.55$  in Supplementary Materials. Further estimation of these values  
517 (Mudd et al., 2018) could improve the accuracy of the results. Second, in the case of  
518 the Wutai Shan, we refer to the geological and low-temperature thermochronology  
519 studies and assume a  $0.50 \pm 0.25$  mm/yr erosion rate at the northern margin of the  
520 Wutai Shan (i.e., the footwall of the North Wutai Shan fault). Combining with the  
521 present-day  $k_{sn}$ , we calculate the erosion coefficient ( $K$ ) and derive the migration rates  
522 of the drainage divide. If the present-day erosion rate deviates from the assumption,  
523 errors would be inevitable in the results. Moreover, the horizontal and vertical errors  
524 of the DEM data, as well as the calculation errors in slope, upstream area and channel  
525 steepness can also affect the reliability of the results. In the case study of the  
526 Yingwang Shan, the lush vegetation may bring errors to the DEM data based on the  
527 SfM technology. The application of airborne light detection and ranging (LiDAR)  
528 technology may help reduce this error. Future studies should take these challenges  
529 into account and overcome them.



530

531 **Figure 6.** (A) Drainage basin in the northern Wutai Shan. (B)  $\chi$ -plots of channel profiles  
 532 in the drainage basin, using  $A_0 = 1 \text{ m}^2$  and  $m/n = 0.35, 0.45,$  and  $0.55$ . The  $\chi$ -plots show  
 533 the best choice of  $m/n$  is  $0.45$ , because the tributaries have systematically higher ( $m/n$   
 534  $= 0.35$ ) or lower ( $m/n = 0.55$ ) elevations than the main stem for other values of  $m/n$   
 535 (excluding the channels in the headwaters).

536

## 537 **5. Conclusions**

538 We have developed a new method (called the "channel-head-point method") to  
 539 calculate the migration rate of drainage divides based on channel-head parameters. We  
 540 have also improved the previously proposed "channel-head-segment method" (Zhou  
 541 et al., 2022a) to adapt the theory to areas where the parameters of channel-heads can  
 542 be accurately determined.

543 Using the new methods and high-resolution topographic data, we determined the  
544 exact locations of the channel heads on both sides of the drainage divide and  
545 quantified the drainage-divide migration rates in two natural cases in North China:  
546 Wutai Shan in the Shanxi Rift, and Yingwang Shan in the Loess Plateau. The  
547 migration rates of the study sites in the Wutai Shan are 0.21-0.27 mm/yr  
548 (northwestward). The rates are close to zero in the Yingwang Shan.

549 Based on the locations of the channel heads and the uplift gradient of the Wutai  
550 Shan, we calculated the cross-divide difference in the uplift rate at the channel heads  
551 ( $\Delta U_{ch}$ ), which is taken into account in the calculation of the drainage-divide migration  
552 rate for the first time. If  $\Delta U_{ch}$  is overlooked, the drainage-divide migration rate of the  
553 study sites in the Wutai Shan will be underestimated by ~4%. Our study highlights  
554 that  $\Delta U_{ch}$  should be considered in the assessment of drainage divide stability based on  
555 the cross-divide difference in channel-head parameters.

556

557 **Data availability.** The analysis of data is based on the Matlab toolbox TAK (Forte  
558 and Whipple, 2019) and TopoToolbox (Schwanghart and Scherler, 2014). The  
559 topography data (ALOS DEM) is downloaded from the Alaska Satellite Facility  
560 (ASF) Data Search (<https://search.asf.alaska.edu/>). The high-resolution DEM of the  
561 two study areas, the Wutai Shan and the Yingwang Shan, can be downloaded from  
562 OpenTopography (<https://doi.org/10.5069/G98C9TGT>).

563 **Acknowledgements.** We would like to thank the Editor Simon Mudd, the  
564 Reviewer Thomas Bernard, and an anonymous reviewer whose suggestions have



565 greatly improved the paper.

566 **Financial support.** This study is supported by the CAS Pioneer Hundred Talents  
567 Program (E2K2010010) and the Fundamental Research Funds for the State Key  
568 Laboratory of Earthquake Dynamics (LED2021A02).

569 **Competing interests.** The authors declare that they have no conflict of interest.

570 **Author contributions.** XT and CZ contributed to the design of the research  
571 scheme. CZ performed the geomorphic analyses. CZ, XT, and FS carried out field  
572 data collection. CZ, XT, YL, and FS contributed to the text and reviewed the paper.

573

## 574 **References**

- 575 Authemayou, C., Brocard, G., Delcaillau, B., Molliex, S., Pedoja, K., Husson, L.,  
576 Aribowo, S., and Cahyarini, S. Y.: Unraveling the roles of asymmetric uplift,  
577 normal faulting and groundwater flow to drainage rearrangement in an emerging  
578 karstic landscape, *Earth Surface Processes and Landforms*, 43(9), 1885-1898,  
579 <https://doi.org/10.1002/esp.4363>, 2018.
- 580 Beeson, H. W., McCoy, S. W., and Keen-Zebert, A.: Geometric disequilibrium of river  
581 basins produces long-lived transient landscapes, *Earth Planet Sc. Lett.*, 475, 34-  
582 43, <https://doi.org/10.1016/j.epsl.2017.07.010>, 2017.
- 583 Bernard, T., Sinclair, H. D., Gailleton, B., and Fox, M.: Formation of Longitudinal  
584 River Valleys and the Fixing of Drainage Divides in Response to Exhumation of  
585 Crystalline Basement, *Geophys. Res. Lett.*, 48,

586 <https://doi.org/10.1029/2020gl092210>, 2021.

587 Bian, S., Tan, X., Liu, Y., Fan, S., Gong, J., Zhou, C., Shi, F., and Murphy, M. A.:  
588 Orographic rainfall drives the Himalaya drainage divide to move north,  
589 *Geomorphology*, 108952, <https://doi.org/10.1016/j.geomorph.2023.108952>,  
590 2024.

591 Bonnet, S.: Shrinking and splitting of drainage basins in orogenic landscapes from  
592 the migration of the main drainage divide, *Nature Geoscience*, 2, 766-771,  
593 <https://doi.org/10.1038/ngeo666>, 2009.

594 Bookhagen, B., and Strecker, M. R.: Spatiotemporal trends in erosion rates across a  
595 pronounced rainfall gradient: Examples from the southern Central Andes, *Earth  
596 Planet Sc. Lett.*, 327-328, 97-110, <https://doi.org/10.1016/j.epsl.2012.02.005>,  
597 2012.

598 Braun, J.: A review of numerical modeling studies of passive margin escarpments  
599 leading to a new analytical expression for the rate of escarpment migration  
600 velocity, *Gondwana Research*, 53, 209-224,  
601 <https://doi.org/10.1016/j.gr.2017.04.012>, 2018.

602 Burbank, D. W., Leland, J., Fielding, E., Anderson, R. S., Brozovic, N., Reid, M. R.,  
603 and Duncan, C.: Bedrock incision, rock uplift and threshold hillslopes in the  
604 northwestern Himalayas, *Nature*, 379, 505–510,  
605 <https://doi.org/10.1038/379505a0>, 1996.

606 Burbank, D. W., and Anderson, R. S.: *Tectonic Geomorphology*, Blackwell Science,  
607 Massachusetts p. 274, 2001.

608 Carson, M. A., and Kirkby, M. J.: Hillslope form and process, New York, Cambridge  
609 University Press, 475, 1972.

610 Chen, C.-Y., Willett, S. D., Christl, M., and Shyu, J. B. H.: Drainage basin dynamics  
611 during the transition from early to mature orogeny in Southern Taiwan, Earth  
612 Planet Sc. Lett. 562, <https://doi.org/10.1016/j.epsl.2021.116874>, 2021.

613 Clark, M. K., Schoenbohm, L. M., Royden, L. H., Whipple, K. X., Burchfiel, B. C.,  
614 Zhang, X., Tang, W., Wang, E., and Chen, L.: Surface uplift, tectonics, and  
615 erosion of eastern Tibet from large-scale drainage patterns, Tectonics 23, 1-20,  
616 <https://doi.org/10.1029/2002tc001402>, 2004.

617 Clift, P. D., and Blusztajn, J.: Reorganization of the western Himalayan river system  
618 after five million years ago, Nature, 438, 1001-1003,  
619 <https://doi.org/10.1038/nature04379>, 2005.

620 Clinkscales, C., Kapp, P., and Wang, H.: Exhumation history of the north-central  
621 Shanxi Rift, North China, revealed by low-temperature thermochronology, Earth  
622 Planet Sc Lett 536, 116146, <https://doi.org/10.1016/j.epsl.2020.116146>, 2020.

623 Clubb, F. J., Mudd, S. M., Milodowski, D. T., Hurst, M. D., and Slater, L. J.:  
624 Objective extraction of channel heads from high-resolution topographic data,  
625 Water Resources Research 50, 4283-4304,  
626 <https://doi.org/10.1002/2013wr015167>, 2014.

627 Crosby, B. T., and Whipple, K. X.: Knickpoint initiation and distribution within  
628 fluvial networks: 236 waterfalls in the Waipaoa River, North Island, New  
629 Zealand, Geomorphology, 82, 16-38,

630 <https://doi.org/10.1016/j.geomorph.2005.08.023>, 2006.

631 Dahlquist, M. P., West, A. J., and Li, G.: Landslide-driven drainage divide migration,  
632 *Geology*, 46, 403-406, <https://doi.org/10.1130/g39916.1>, 2018.

633 Deng, B., Chew, D., Mark, C., Liu, S., Cogné, N., Jiang, L., O’Sullivan, G., Li, Z.,  
634 and Li, J.: Late Cenozoic drainage reorganization of the paleo-Yangtze river  
635 constrained by multi-proxy provenance analysis of the Paleo-lake Xigeda, *GSA*  
636 *Bulletin*, <https://doi.org/10.1130/b35579.1>, 2020.

637 DiBiase, R. A., Whipple, K. X., Heimsath, A. M., Ouimet, W. B.: Landscape form and  
638 millennial erosion rates in the San Gabriel Mountains, CA, *Earth Planet Sc. Lett.*,  
639 289, 134-144, <https://doi.org/10.1016/j.epsl.2009.10.036>, 2010.

640 Duvall, A.: Tectonic and lithologic controls on bedrock channel profiles and processes  
641 in coastal California, *J. Geophys. Res.*, 109,  
642 <https://doi.org/10.1029/2003jf000086>, 2004.

643 Forte, A. M., and Whipple, K. X.: Criteria and tools for determining drainage divide  
644 stability, *Earth Planet Sc. Lett.*, 493, 102–117,  
645 <https://doi.org/10.1016/j.epsl.2018.04.026>, 2018.

646 Forte, A. M., and Whipple, K. X.: Short communication: The Topographic Analysis  
647 Kit (TAK) for TopoToolbox, *Earth Surface Dynamics* 7, 87–95,  
648 <https://doi.org/10.5194/esurf-7-87-2019>, 2019.

649 Forte, A. M., Yanites, B. J., and Whipple, K. X.: Complexities of landscape evolution  
650 during incision through layered stratigraphy with contrasts in rock strength,  
651 *Earth Surface Processes and Landforms*, 41, 1736-1757,

652 <https://doi.org/10.1002/esp.3947>, 2016.

653 Fu, B.: Soil erosion and its control in the loess plateau of China, *Soil Use and*  
654 *Management*, 5, 76-82, <https://doi.org/10.1111/j.1475-2743.1989.tb00765.x>,  
655 1989.

656 Gallen, S. F.: Lithologic controls on landscape dynamics and aquatic species  
657 evolution in post-orogenic mountains, *Earth Planet Sc. Lett.*, 493, 150-160,  
658 <https://doi.org/10.1016/j.epsl.2018.04.029>, 2018.

659 Godard, V., Dosseto, A., Fleury, J., Bellier, O., and Siame, L.: Transient landscape  
660 dynamics across the Southeastern Australian Escarpment, *Earth Planet Sc. Lett.*,  
661 506, 397-406, <https://doi.org/10.1016/j.epsl.2018.11.017>, 2019.

662 Godard, V., Hippolyte, J.-C., Cushing, E., Espurt, N., Fleury, J., Bellier, O., and  
663 Ollivier, V.: Hillslope denudation and morphologic response to a rock uplift  
664 gradient, *Earth Surface Dynamics*, 8, 221-243, [https://doi.org/10.5194/esurf-8-](https://doi.org/10.5194/esurf-8-221-2020)  
665 [221-2020](https://doi.org/10.5194/esurf-8-221-2020), 2020.

666 Goren, L., Fox, M., and Willett, S. D.: Tectonics from fluvial topography using formal  
667 linear inversion: Theory and applications to the Inyo Mountains, California,  
668 *Journal of Geophysical Research: Earth Surface*, 119, 1651-1681,  
669 <https://doi.org/10.1002/2014jgf003079>, 2014.

670 Hancock, G. S., and Anderson, R. S.: Numerical modeling of fluvial strath-terrace  
671 formation in response to oscillating climate, *GSA Bulletin*, 114, 1131-1142,  
672 [https://doi.org/10.1130/0016-7606\(2002\)114<1131:nmofst>2.0.co;2](https://doi.org/10.1130/0016-7606(2002)114<1131:nmofst>2.0.co;2), 2002.

673 He, C., Yang, C. J., Turowski, J. M., Rao, G., Roda-Boluda, D. C., and Yuan, X. P.:

674 Constraining tectonic uplift and advection from the main drainage divide of a  
675 mountain belt, *Nat. Commun.*, 12, 544, [https://doi.org/10.1038/s41467-020-](https://doi.org/10.1038/s41467-020-20748-2)  
676 [20748-2](https://doi.org/10.1038/s41467-020-20748-2), 2021.

677 Hilley, G. E., and Arrowsmith, J. R.: Geomorphic response to uplift along the  
678 Dragon's Back pressure ridge, Carrizo Plain, California, *Geology*, 36,  
679 <https://doi.org/10.1130/g24517a.1>, 2008.

680 Young, H. H., and Hilley, G. E.: Millennial-scale denudation rates of the Santa Lucia  
681 Mountains, California: Implications for landscape evolution in steep, high-relief,  
682 coastal mountain ranges, *GSA Bulletin*, 130 (11-12), 1809–1824,  
683 <https://doi.org/10.1130/B31907.1>, 2018.

684 Hoorn, C., Wesselingh, F. P., Steege, H. T., Bermudez, M. A., and Antonelli, A.:  
685 Amazonia Through Time: Andean Uplift, Climate Change, Landscape Evolution,  
686 and Biodiversity, *Science*, 330, 927-931,  
687 <https://doi.org/10.1126/science.1194585>, 2010.

688 Hoskins, A. M., Attal, M., Mudd, S. M., and Castillo, M.: Topographic Response to  
689 Horizontal Advection in Normal Fault-Bound Mountain Ranges, *Journal of*  
690 *Geophysical Research: Earth Surface*, 128,  
691 <https://doi.org/10.1029/2023jf007126>, 2023.

692 Howard, A. D., Dietrich, W. E., and Seidl, M. A.: Modeling fluvial erosion on  
693 regional to continental scales, *Journal of Geophysical Research: Solid Earth*, 99,  
694 13971-13986, <https://doi.org/10.1029/94jb00744>, 1994.

695 Howard, A. D., and Kerby, G.: Channel changes in badlands, *Geological Society of*

696 America Bulletin, 94, 739, <https://doi.org/10.1130/0016->  
697 [7606\(1983\)94<739:CCIB>2.0.CO;2](https://doi.org/10.1130/0016-7606(1983)94<739:CCIB>2.0.CO;2), 1983.

698 Hu, K., Fang, X., Ferrier, K. L., Granger, D. E., Zhao, Z., and Ruetenik, G. A.:  
699 Covariation of cross-divide differences in denudation rate and  $\chi$ : Implications for  
700 drainage basin reorganization in the Qilian Shan, northeast Tibet, Earth Planet  
701 Sc. Lett., 562, 116812, <https://doi.org/10.1016/j.epsl.2021.116812>, 2021.

702 Hurst, M. D., Mudd, S. M., Walcott, R., Attal, M., and Yoo, K.: Using hilltop  
703 curvature to derive the spatial distribution of erosion rates, Journal of  
704 Geophysical Research: Earth Surface, 117,  
705 <https://doi.org/10.1029/2011jf002057>, 2012.

706 Jiao, R., Fox, M., and Yang, R.: Late Cenozoic erosion pattern of the eastern margin  
707 of the Sichuan Basin: Implications for the drainage evolution of the Yangtze  
708 River, Geomorphology, 398, 108025,  
709 <https://doi.org/10.1016/j.geomorph.2021.108025>, 2022.

710 Kirby, E., and Whipple, K.: Quantifying differential rock-uplift rates via stream  
711 profile analysis, Geology, 29, 415-418, <https://doi.org/10.1130/0091->  
712 [7613\(2001\)029<0415:Qdrurv>2.0.Co;2](https://doi.org/10.1130/0091-7613(2001)029<0415:Qdrurv>2.0.Co;2), 2001.

713 Kirby, E., Whipple, K., Tang, W., and Chen, Z.: Distribution of active rock uplift  
714 along the eastern margin of the Tibetan Plateau: Inferences from bedrock channel  
715 longitudinal profiles, Journal of Geophysical Research, 108(B4), 2217,  
716 <https://doi.org/10.1029/2001JB000861>, 2003.

717 Kirby, E., and Whipple, K. X.: Expression of active tectonics in erosional landscapes,

718 J. Struct. Geol., 44, 54-75, <https://doi.org/10.1016/j.jsg.2012.07.009>, 2012.

719 Kirkpatrick, H. M., Moon, S., Yin, A., and Harrison, T. M.: Impact of fault damage on  
720 eastern Tibet topography, *Geology*, 48, <https://doi.org/10.1130/g48179.1>, 2020.

721 Ma, Z., Zhang, H., Wang, Y., Tao, Y., and Li, X.: Inversion of Dadu River Bedrock  
722 Channels for the Late Cenozoic Uplift History of the Eastern Tibetan Plateau,  
723 *Geophys. Res. Lett.*, 47, <https://doi.org/10.1029/2019gl086882>, 2020.

724 Mandal, S. K., Lupker, M., Burg, J.-P., Valla, P. G., Haghypour, N., and Christl, M.:  
725 Spatial variability of  $^{10}\text{Be}$ -derived erosion rates across the southern Peninsular  
726 Indian escarpment: A key to landscape evolution across passive margins, *Earth  
727 Planet Sc. Lett.*, 425, 154-167, <https://doi.org/10.1016/j.epsl.2015.05.050>, 2015.

728 Molnar, P., and England, P.: Late Cenozoic uplift of mountain ranges and global  
729 climate change: chicken or egg? *Nature*, 346, 29-34,  
730 [https://doi.org/10.1038\\_346029a0](https://doi.org/10.1038_346029a0), 1990.

731 Mudd, S. M., Clubb, F. J., Gailleton, B., and Hurst, M. D.: How concave are river  
732 channels? *Earth Surface Dynamics*, 6, 505-523, [https://doi.org/10.5194/esurf-6-  
733 505-2018](https://doi.org/10.5194/esurf-6-505-2018), 2018.

734 Musher, L. J., Giakoumis, M., Albert, J., Rio, G. D., Rego, M., Thom, G., Aleixo, A.,  
735 Ribas, C. C., Brumfield, R. T., and Smith, B. T.: River network rearrangements  
736 promote speciation in lowland Amazonian birds, Cold Spring Harbor Laboratory,  
737 <https://doi.org/10.1126/sciadv.abn1099>, 2021.

738 Perron, J. T., Dietrich, W. E., and Kirchner, J. W.: Controls on the spacing of first-  
739 order valleys, *J. Geophys. Res.*, 113, <https://doi.org/10.1029/2007jf000977>,



740 2008.

741 Perron, J. T., and Royden, L.: An integral approach to bedrock river profile analysis,  
742 Earth Surface Processes and Landforms, 38, 570-576,  
743 <https://doi.org/10.1002/esp.3302>, 2012.

744 Pritchard, D., Roberts, G. G., White, N. J., and Richardson, C. N.: Uplift histories  
745 from river profiles, Geophys. Res. Lett., 36,  
746 <https://doi.org/10.1029/2009gl040928>, 2009.

747 Royden, L., Clark, M., and Whipple, K.: Evolution of river elevation profiles by  
748 bedrock incision: Analytical solutions for transient river profiles related to  
749 changing uplift and precipitation rates, Eos Trans, AGU, 81, 2000.

750 Safran, E. B., Bierman, P. R., Aalto, R., Dunne, T., Whipple, K. X., and Caffee, M.:  
751 Erosion rates driven by channel network incision in the Bolivian Andes, Earth  
752 Surface Processes and Landforms, 30, 1007-1024,  
753 <https://doi.org/10.1002/esp.1259>, 2005.

754 Sassolas-Serrayet, T., Cattin, R., Ferry, M., Godard, V., and Simoes, M.: Estimating  
755 the disequilibrium in denudation rates due to divide migration at the scale of  
756 river basins, Earth Surface Dynamics, 7, 1041-1057,  
757 <https://doi.org/10.5194/esurf-7-1041-2019>, 2019.

758 Scheingross, J. S., Limaye, A. B., McCoy, S. W., and Whittaker, A. C.: The shaping of  
759 erosional landscapes by internal dynamics, Nature Reviews Earth &  
760 Environment, 1, 661-676, <https://doi.org/10.1038/s43017-020-0096-0>, 2020.

761 Scherler, D., and Schwanghart, W.: Drainage divide networks – Part 2: Response to

762 perturbations, *Earth Surface Dynamics*, 8, 261-274,  
763 <https://doi.org/10.5194/esurf-8-261-2020>, 2020.

764 Schildgen, T. F., van der Beek, P. A., D'Arcy, M., Roda-Boluda, D., Orr, E. N., and  
765 Wittmann, H.: Quantifying drainage-divide migration from orographic rainfall  
766 over geologic timescales: Sierra de Aconquija, southern Central Andes, *Earth*  
767 *Planet Sc. Lett.*, 579, 117345, <https://doi.org/10.1016/j.epsl.2021.117345>, 2022.

768 Schlunegger, F., Norton, K. P., and Zeilinger, G.: Climatic Forcing on Channel  
769 Profiles in the Eastern Cordillera of the Coroico Region, Bolivia, *The Journal of*  
770 *Geology*, 119, 97-107, <https://doi.org/10.1086/657407>, 2011.

771 Schwanghart, W., and Scherler, D.: Short Communication: TopoToolbox 2 –  
772 MATLAB-based software for topographic analysis and modeling in Earth  
773 surface sciences, *Earth Surface Dynamics*, 2, 1-7, [https://doi.org/10.5194/esurf-](https://doi.org/10.5194/esurf-2-1-2014)  
774 [2-1-2014](https://doi.org/10.5194/esurf-2-1-2014), 2014.

775 Shelef, E., and Goren, L.: The rate and extent of wind-gap migration regulated by  
776 tributary confluences and avulsions, *Earth Surface Dynamics*, 9(4), 687-700,  
777 <https://doi.org/10.5194/esurf-9-687-2021>, 2021.

778 Shi, F., Tan, X., Zhou, C., and Liu, Y.: Impact of asymmetric uplift on mountain  
779 asymmetry: Analytical solution, numerical modeling, and natural examples,  
780 *Geomorphology*, 389, 107862, <https://doi.org/10.1016/j.geomorph.2021.107862>,  
781 2021.

782 Shi, W., Dong, S., and Hu, J.: Neotectonics around the Ordos Block, North China: A  
783 review and new insights, *Earth-Science Reviews*, 200, 102969,

784 <https://doi.org/10.1016/j.earscirev.2019.102969>, 2020.

785 Stark, C. P.: Oscillatory motion of drainage divides, *Geophys. Res. Lett.*, 37,

786 <https://doi.org/10.1029/2009gl040851>, 2010.

787 Stock, J. D., and Dietrich, W. E.: Erosion of steepland valleys by debris flows,

788 *Geological Society of America Bulletin*, 118, 1125-1148,

789 <https://doi.org/10.1130/b25902.1>, 2006.

790 Stokes, M. F., Larsen, I. J., Goldberg, S. L., McCoy, S. W., Prince, P. P., and Perron, J.

791 T.: The Erosional Signature of Drainage Divide Motion Along the Blue Ridge

792 Escarpment, *Journal of Geophysical Research: Earth Surface*, 128,

793 <https://doi.org/10.1029/2022jf006757>, 2023.

794 Struth, L., Teixell, A., Owen, L. A., and Babault, J.: Plateau reduction by drainage

795 divide migration in the Eastern Cordillera of Colombia defined by morphometry

796 and <sup>10</sup>Be terrestrial cosmogenic nuclides, *Earth Surface Processes and*

797 *Landforms*, 42, 1155-1170, <https://doi.org/10.1002/esp.4079>, 2017.

798 Su, P., He, H., Tan, X., Liu, Y., Shi, F., and Kirby, E.: Initiation and Evolution of the

799 Shanxi Rift System in North China: Evidence From Low-Temperature

800 Thermochronology in a Plate Reconstruction Framework, *Tectonics*, 40,

801 <https://doi.org/10.1029/2020tc006298>, 2021.

802 Su, Q., Wang, X., Lu, H., and Xie, H.: Dynamic Divide Migration as a Response to

803 Asymmetric Uplift: An Example from the Zhongtiao Shan, North China, *Remote*

804 *Sensing*, 12, <https://doi.org/10.3390/rs12244188>, 2020.

805 Tucker, G. E., and Bras, R. L.: Hillslope processes, drainage density, and landscape

806 morphology, *Water Resources Research*, 34, 2751-2764,  
807 <https://doi.org/10.1029/98wr01474>, 1998.

808 Tucker, G. E., and Slingerland, R.: Drainage basin responses to climate change, *Water*  
809 *Resources Research*, 33, 2031-2047, <https://doi.org/10.1029/97wr00409>, 1997.

810 Vacherat, A., Bonnet, S., and Mouthereau, F.: Drainage reorganization and divide  
811 migration induced by the excavation of the Ebro basin (NE Spain), *Earth Surface*  
812 *Dynamics*, 6(2), 369-387, <https://doi.org/10.5194/esurf-6-369-2018>, 2018.

813 Wang, Y., Liu, C., Zheng, D., Zhang, H., Yu, J., Pang, J., Li, C., and Hao, Y.:  
814 Multistage Exhumation in the Catchment of the Anninghe River in the SE  
815 Tibetan Plateau: Insights From Both Detrital Thermochronology and  
816 Topographic Analysis, *Geophys. Res. Lett.*, 48,  
817 <https://doi.org/10.1029/2021gl092587>, 2021.

818 Waters, J. M., Craw, D., Youngson, J. H., and Wallis, G. P.: Genes meet geology: fish  
819 phylogeographic pattern reflects ancient, rather than modern, drainage  
820 connections, *Evolution*, 55, 1844-1851, [https://doi.org/10.1111/j.0014-](https://doi.org/10.1111/j.0014-3820.2001.tb00833.x)  
821 [3820.2001.tb00833.x](https://doi.org/10.1111/j.0014-3820.2001.tb00833.x), 2001.

822 Wei, Z., Arrowsmith, J. R., and He, H.: Evaluating fluvial terrace riser degradation  
823 using LiDAR-derived topography: An example from the northern Tian Shan,  
824 China, *Journal of Asian Earth Sciences*, 105, 430-442,  
825 <https://doi.org/10.1016/j.jseaes.2015.02.016>, 2015.

826 Whipple, K. X.: Fluvial landscape response time: how plausible is steady-state  
827 denudation? *Am. J. Sci.*, 301, 313-325, <https://doi.org/10.2475/ajs.301.4-5.313>,

828 2001.

829 Whipple, K. X.: The influence of climate on the tectonic evolution of mountain belts,  
830 Nature Geoscience, 2, 97-104, <https://doi.org/10.1038/ngeo413>, 2009.

831 Whipple, K. X., Forte, A. M., DiBiase, R. A., Gasparini, N. M., and Ouimet, W. B.:  
832 Timescales of landscape response to divide migration and drainage capture:  
833 Implications for the role of divide mobility in landscape evolution, Journal of  
834 Geophysical Research: Earth Surface, 122, 248-273,  
835 <https://doi.org/10.1002/2016JF003973>, 2017.

836 Whipple, K. X., Kirby, E., and Brocklehurst, S. H.: Geomorphic limits to climate-  
837 induced increases in topographic relief, Nature, 401, 39-43,  
838 <https://doi.org/10.1038/43375>, 1999.

839 Willett, S. D., McCoy, S. W., Perron, J. T., Goren, L., and Chen, C. Y.: Dynamic  
840 reorganization of river basins, Science, 343, 1117,  
841 <https://doi.org/10.1126/science.1248765>, 2014.

842 Willett, S. D., McCoy, S. W., and Beeson, H. W.: Transience of the North American  
843 High Plains landscape and its impact on surface water, Nature, 561, 528-532,  
844 <https://doi.org/10.1038/s41586-018-0532-1>, 2018.

845 Wobus, C., Whipple, K. X., Kirby, E., Snyder, N., Johnson, J., Spyropolou, K.,  
846 Crosby, B., and Sheehan, D.: Tectonics from topography: Procedures, promise,  
847 and pitfalls, Tectonics, Climate, and Landscape Evolution, 55-74,  
848 [https://doi.org/10.1130/2006.2398\(04\)](https://doi.org/10.1130/2006.2398(04)) , 2006.

849 Wu, Y., Yang, R., He, C., and He, J.: Caution on determining divide migration from

850 cross-divide contrast in  $\chi$ , *Geological Journal*, 57(12),  
851 <https://doi.org/10.1002/gj.4530>, 2022.

852 Xiong, L.-Y., Tang, G.-A., Li, F.-Y., Yuan, B.-Y., and Lu, Z.-C.: Modeling the  
853 evolution of loess-covered landforms in the Loess Plateau of China using a DEM  
854 of underground bedrock surface, *Geomorphology*, 209, 18-26.  
855 <https://doi.org/10.1016/j.geomorph.2013.12.009>, 2014.

856 Xu, X., Ma, X., and Deng, Q.: Neotectonic activity along the Shanxi rift system,  
857 China, *Tectonophysics*, 219, 305-325, [https://doi.org/10.1016/0040-  
858 1951\(93\)90180-R](https://doi.org/10.1016/0040-1951(93)90180-R), 1993.

859 Yan, M.-J., He, Q.-Y., Yamanaka, N., and Du, S.: Location, Geology and Landforms  
860 of the Loess Plateau, in: Tsunekawa, A., Liu, G., Yamanaka, N., Du, S. (Eds.),  
861 Restoration and development of the degraded Loess Plateau, China, Springer  
862 Japan, 3-22, <https://doi.org/10.1007/978-4-431-54481-4>, 2014.

863 Yang, R., Suhail, H. A., Gourbet, L., Willett, S. D., Fellin, M. G., Lin, X., Gong, J.,  
864 Wei, X., Maden, C., Jiao, R., and Chen, H.: Early Pleistocene drainage pattern  
865 changes in Eastern Tibet: Constraints from provenance analysis,  
866 thermochronometry, and numerical modeling, *Earth Planet Sc. Lett.*, 531, 1-10,  
867 <https://doi.org/10.1016/j.epsl.2019.115955>, 2019.

868 Ye, Y., Tan, X., and Zhou, C.: Initial topography matters in drainage divide migration  
869 analysis: Insights from numerical simulations and natural examples,  
870 *Geomorphology*, 409, 108266, <https://doi.org/10.1016/j.geomorph.2022.108266>,  
871 2022.

872 Yin, A.: Cenozoic tectonic evolution of Asia: A preliminary synthesis, *Tectonophysics*  
873 488, 293-325, <https://doi.org/10.1016/j.tecto.2009.06.002>, 2010.

874 Zemplak, T. S., Habit, E. M., Walde, S. J., Battini, M. A., Adams, E. D. M., and  
875 Ruzzante, D. E.: Across the southern Andes on fin: glacial refugia, drainage  
876 reversals and a secondary contact zone revealed by the phylogeographical signal  
877 of *Galaxias platei* in Patagonia, *Molecular Ecology*, 17, 5049-5061,  
878 <https://doi.org/10.1111/j.1365-294X.2008.03987.x>, 2008.

879 Zeng, X., and Tan, X.: Drainage divide migration in response to strike-slip faulting:  
880 An example from northern Longmen Shan, eastern Tibet, *Tectonophysics*, 848,  
881 229720, <https://doi.org/10.1016/j.tecto.2023.229720>, 2023.

882 Zhao, X., Zhang, H., Hetzel, R., Kirby, E., Duvall, A.R., Whipple, K. X., Xiong, J.,  
883 Li, Y., Pang, J., Wang, Y., Wang, P., Liu, K., Ma, P., Zhang, B., Li, X., Zhang, J.,  
884 and Zhang, P.: Existence of a continental-scale river system in eastern Tibet  
885 during the late Cretaceous-early Palaeogene, *Nat. Commun.*, 12, 7231,  
886 <https://doi.org/10.1038/s41467-021-27587-9>, 2021.

887 Zhou, C., Tan, X., Liu, Y., Lu, R., Murphy, M. A., He, H., Han, Z., and Xu, X.:  
888 Ongoing westward migration of drainage divides in eastern Tibet, quantified  
889 from topographic analysis, *Geomorphology*, 402, 108123,  
890 <https://doi.org/10.1016/j.geomorph.2022.108123>, 2022a.

891 Zhou, C., Tan, X., Liu, Y., and Shi, F.: A cross-divide contrast index (C) for assessing  
892 controls on the main drainage divide stability of a mountain belt,  
893 *Geomorphology*, 398, 108071, <https://doi.org/10.1016/j.geomorph.2021.108071>,



894 2022b.

895 Zhou, C., and Tan, X.: Quantifying the influence of asymmetric uplift, base level  
896 elevation, and erodibility on cross-divide  $\chi$  difference, *Geomorphology*, 427,  
897 108634, <https://doi.org/10.1016/j.geomorph.2023.108634>, 2023.

898 Zondervan, J. R., Stokes, M., Boulton, S. J., Telfer, M. W., and Mather, A. E.: Rock  
899 strength and structural controls on fluvial erodibility: Implications for drainage  
900 divide mobility in a collisional mountain belt, *Earth Planet Sc. Lett.*, 538,  
901 <https://doi.org/10.1016/j.epsl.2020.116221>, 2020.